ADVANCED MATERIALS INTERFACES
www.advmatinterfaces.de

Check for updates

Silver Nanoparticle-Decorated Reduced Graphene Oxide Nanomaterials Exert Membrane Stress and Induce Immune Response to Inhibit the Early Phase of HIV-1 Infection

Soumajit Mukherjee, Zuzana Bytesnikova, Sophie Martin, Pavel Svec, Andrea Ridoskova, Jana Pekarkova, Cendrine Seguin, Jean-Luc Weickert, Nadia Messaddeq, Yves Mély, Lukas Richtera, Halina Anton, and Vojtech Adam**

Graphene-based 2D nanomaterials exhibit unique physicochemical, electric, and optical properties that facilitate applications in a wide range of fields including material science, electronics, and biotechnology. Recent studies have shown that graphene oxide (GO) and reduced graphene oxide (rGO) exhibit antimicrobial effects on bacteria and viruses. While the bactericidal activity of graphene-based nanomaterials is related to mechanical and oxidative damage to bacterial membranes, their antiviral activity has been less explored. Currently available experimental data are limited and suggest mechanical disruption of viral particles prior to infection. In this study, the antiviral properties of reduced GO-based nanocomposites decorated with Ag nanoparticles (rGO-Ag) are evidenced against human immunodeficiency virus-1 pseudovirus used as an enveloped virus model. By combining biochemical and original single virus imaging approaches, it is shown that rGO-Ag induces peroxidation of pseudoviral lipid membrane and that consequent alteration of membrane properties leads to a reduction in cell entry. In addition, rGO-Ag is found to be efficiently internalized in the host cell leading to the elevated expression of pro-inflammatory cytokines. Altogether, the presented results shed new light on the mechanisms of rGO-Ag antiviral properties and confirm the high potential of graphene derivatives as an antimicrobial material for biomedical applications.

1. Introduction

Graphene oxide (GO) has been at the forefront of carbon nanomaterial research over the past two decades. Due to their unique properties, such as a large surface area, high tensile strength, the presence of modifiable surface groups, and good biocompatibility, graphene derivatives have been used to expand several areas of research including electronics, materials science, nonlinear optics, and biotechnologies.[1–8] GO is formally derived from graphene, which is a single layer of carbon atoms bonded in a 2D hexagonal lattice.[9,10] The chemical oxidation and exfoliation of graphite produce GO-exhibiting surface groups, such as carboxyl, hydroxyl, epoxy, and carbonyl groups, that offer an excellent opportunity to covalently bind biomolecules, drugs, or fluorophores. The exact composition and number of these groups are variable and depend on the synthesis pathway.[2,11] The chemical

S. Mukherjee, Z. Bytesnikova, P. Svec, A. Ridoskova, L. Richtera, V. Adam
Department of Chemistry and Biochemistry
Mendel University in Brno
Zemedelska 1, Brno 61300, Czech Republic
E-mail: vojtech.adam@mendelu.cz

S. Martin, Y. Mély, H. Anton
Laboratory of Bioimaging and Pathologies
CNRS UMR 7021
Faculty of Pharmacy
University of Strasbourg
74, route du Rhin, Illkirch-Graffenstaden 67400, France
E-mail: halina.anton@unistra.fr

The ORCID identification number(s) for the author(s) of this article can be found under https://doi.org/10.1002/admi.202201996.

© 2022 The Authors. Advanced Materials Interfaces published by Wiley-VCH GmbH. This is an open access article under the terms of the Creative Commons Attribution License, which permits use, distribution and reproduction in any medium, provided the original work is properly cited.

DOI: 10.1002/admi.202201996

J. Pekarkova
Department of Microelectronics
Faculty of Electrical Engineering and Communication
Brno University of Technology
Technicka 3058/10, Brno 61600, Czech Republic

J. Pekarkova, V. Adam
Central European Institute of Technology
Brno University of Technology
Purkynova 656/123, Brno 61200, Czech Republic

C. Seguin
Laboratory of Design and Application of Bioactive Molecules
CNRS UMR 7199
Faculty of Pharmacy
University of Strasbourg
74, route du Rhin, Illkirch-Graffenstaden 67400, France

J.-L. Weickert, N. Messaddeq
Imaging Center
Institute of Genetics and Molecular and Cellular Biology (IGBMC)
1 Rue Laurent Fries, Illkirch-Graffenstaden 67400, France

21967350, 2023, 6, Downloaded from https://onlinelibrary.wiley.com/doi/10.1002/admi.202201996 by Technical University In Brno, Wiley Online Library on [04/08/2023]. See the Terms and Conditions (https://onlinelibrary.wiley.com/terms-and-conditions) on Wiley Online Library for rules of use; OA articles are governed by the applicable Creative Commons License

reduction of GO reduces the surface functional groups to produce reduced graphene oxide (rGO).[12,13] The atomic-thin layer 2D structure of GO-derived materials is particularly beneficial for biomedical use as the flexibility of the nanomaterial allows it to fold in tight spaces in biological systems.

Recent studies have shown that GO and rGO exhibit inhibiting effects on bacteria as well as viruses.[14–19] The biocidal activity of GO was first described in 2010.[20,21] Since, the effects of graphene-based materials were investigated for a variety of microorganisms, including *Pseudomonas aeruginosa*, *Escherichia coli*, herpes simplex virus (HSV), pseudorabies virus (PRV), porcine epidemic diarrhea virus (PEDV), porcine reproductive and respiratory syndrome virus (PRRSV), and severe acute respiratory syndrome coronavirus (SARS CoV-2).[16,17,19,22–25] Despite active research in the field, the underlying mechanisms of the antimicrobial activity of GO-based materials are still debated, possibly because of their dependence on the synthesis paths determining the physicochemical properties of the final materials. The size, charge density, and presence of functional groups determine the interactions with biological molecules and hence their potential biological functions.[19,24]

Several studies have shown that the sharp edges of 2D GO nanosheets damage microbial external membranes (viral envelopes), leading to the release of intracellular content and infection inhibition. This nano-knife concept has been discussed in studies on *E. coli, Staphylococcus aureus*, HSV, PRRSV, and PEDV.[14,16,20,26] Less destructive effects, such as GO attachment to the external membranes and lipid extraction, have also been suggested.[14,19,26–28] Moreover, since GO sheets are flexible, they can envelope bacterial or cellular surfaces, and thus, impede pathogen cell entry.[24,29]

The antimicrobial activities of GO-derived materials can be enhanced by coupling them with silver nanoparticles (Ag NPs). Indeed, Ag NPs have attracted attention due to their antibacterial, antifungal, and antiviral properties.[18,30,31] Interestingly, Ag NPs and multilayer GO have been shown to stimulate cell proliferation and migration, which can be profitable for biomedical applications such as tissue engineering or wound healing.[32,33] However, due to their high chemical reactivity, Ag NPs aggregate or agglomerate in biological media, which reduces their overall efficacy.[34,35] To overcome this limitation, GO is used as a stabilizer that covalently binds Ag NPs through its surface groups. Ag-decorated GO nanocomposites (GO-Ag) show antiviral activities against enveloped (feline coronavirus) and non-enveloped (infectious bursal disease virus) viruses.[36] In a recent report, Du et al. showed that GO-Ag efficiently inhibits PRRSV and PEDV infection by acting on viral particles prior to entry. Transmission electron microscopy (TEM) images of the viral particles incubated with GO-Ag revealed structural damage caused by the sharp edges of the GO sheets. Interestingly, GO-Ag treatment was also reported to stimulate the innate immune response in host cells (MARC-145).[17]

Although the antiviral activities of GO and its derivatives are well established, reports on their inhibitory mechanisms remain rare. In this context, we aimed to depict the antiviral activity of rGO-Ag-based nanomaterials. Human immunodeficiency virus-1 (HIV-1) pseudotyped lentivirus (PSV) was used as enveloped virus model. Compared to the GO-Ag reported in previous antiviral studies, rGO-Ag is more hydrophobic and contains fewer oxygen groups. Therefore, we assume that the interaction with the virus will impact the viral lipid membrane and efficiently inhibit the infectivity of the viral particles. To verify this hypothesis, a series of biochemical and microscopy-based experimental approaches were used to evaluate the effect of rGO-Ag on HIV-1 infection and to unveil the mechanism of this inhibition.

2. Results

2.1. Preparation and Characterization of rGO-Ag

GO sheets were synthesized according to the modified Hummer's method and used as a starting nanomaterial for the preparation of nanocomposites (NCs) with Ag NPs. Figure S1, Supporting Information, shows the scanning electron microscopy (SEM) and atomic force microscopy (AFM) images of the obtained GO as a nanomaterial with a large sheet-like structure and smooth surfaces. **Figure 1**a shows the SEM images of rGO reduced by sodium borohydride in mild (200 mg) and stronger (400 mg) conditions in the presence of silver nitrate for the preparation of two distinct NCs, rGO-Ag_L and rGO-Ag_H. In all images, rGO is observed with Ag NPs distributed on its surface. The TEM images of both NCs confirmed the nanoscale size of the Ag NPs (Figure 1b). Energy-dispersive X-ray spectroscopy (EDS) was used to confirm the elemental compositions of all synthesized nanomaterials (Figure S2, Supporting Information). Elemental mapping of the nanoparticles by TEM and scanning transmission electron microscopy (STEM) is demonstrated in the insets, where green represents silver and red represents carbon (Figures 1c,d).

AFM was used to study the topographies of the synthesized rGO-Ag_L and rGO-Ag_H. **Figure 2**a shows the 2D images of the NCs demonstrating their single-layer character, whereas the 3D images (Figure 2b) demonstrate the thickness of the rGO sheets with distributed Ag NPs. Raman spectroscopy was used to confirm the reduction after the addition of different amounts of sodium borohydride. The D (≈1335 cm^{-1}) and G (1610 cm^{-1}) peaks showed different intensities for rGO-Ag_L and rGO-Ag_H (Figure 2c). The G band is a result of the in-plane vibrations of sp^2-bonded carbon atoms, while the D band is due to the out-of-plane vibrations attributed to the presence of structural defects. The intensity ratio of the D/G bands (I_D/I_G) is thus a measure of the defects in the graphene structure. The I_D/I_G ratio of rGO-Ag_L was lower than that of rGO-Ag_H, indicating a stronger reduction of rGO in the sample, in which more reducing agent was used (**Table 1**).[37]

The Raman spectroscopy data are in accordance with the X-ray photoelectron spectroscopy (XPS) analysis that was performed to determine the rGO-Ag surface composition and the Ag oxidation state. Figure S3, Supporting Information, shows the characteristic wide-scale XPS spectra for the rGO-Ag samples. The high-resolution spectra of the C 1s, O 1s, and Ag 3d regions, presented in **Figure 3**a,b show the covalent bond structures in the nanomaterial. The peak values are indicative of the type of covalent bonds present in the synthesized rGO-Ag samples. The high-resolution spectra of rGO-Ag_L and rGO-Ag_H show three peaks in the C 1s region, indicating the presence of sp^2 carbon at 284.71 and 284.78 eV, C—OH at 286.83 and 286. 90 eV, and C—O—C at 288.21 and 288.28 eV, respectively

© 2022 The Authors. Advanced Materials Interfaces published by Wiley-VCH GmbH

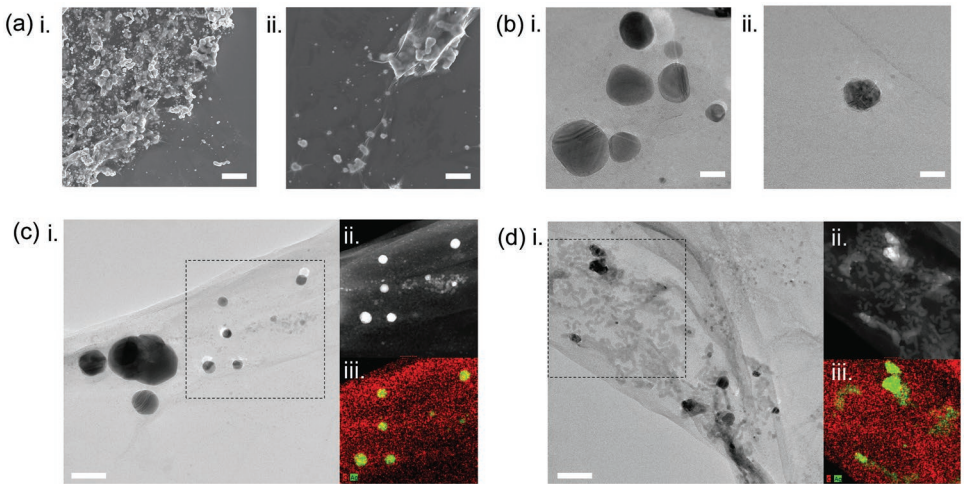

Figure 1. Physical characterization of the synthesized rGO-Ag. a) SEM images of rGO-Ag_L (i) and rGO-Ag_H (ii) showing rGO sheets decorated with Ag NPs, scale bars 2 µm, b) TEM images of rGO-Ag_L (i) and rGO-Ag_H (ii) showing the presence of nanoscale Ag NPs (scale bars 10 nm), c,d) TEM (i), STEM (ii), and EDS (iii) mapping of rGO-Ag_L and rGO-Ag_H, respectively, scale bars 50 nm. The STEM images and EDS mapping show the presence of Ag NPs as bright or green spots, respectively, scale bars 50 nm.

(Figure 3ai,bi).[38] The O 1s regions of rGO-Ag_L and rGO-Ag_H presented two main components: C=O at 531.01 and 531.07 eV and C—OH at 532.61 and 532.67 eV, respectively (Figure 3aii,bii).[39] The high-resolution XPS spectra of the Ag 3d peaks of rGO-Ag_L and rGO-Ag_H showed two peaks attributed to Ag ($3d_{5/2}$) and Ag ($3d_{3/2}$) centered at 368.38, 368.42, 374.38, and 374.38 eV, respectively (Figure 3aiii,biii). The binding energies of these photoelectron peaks are characteristic of metallic Ag, indicating the presence of Ag(0) on the surface of the rGO sheets and confirming the Ag oxidation state.[40] The main chemical species and their atomic concentrations are summarized in Table 1. To evaluate the stability and overall surface charge of the synthesized rGO-Ag nanomaterials, their zeta potential was measured. All rGO-Ag samples were found to possess a strongly negative electric charge, favoring a highly stable NC dispersion (Table 1).

2.2. rGO-Ag NCs Show Effective Virucidal Activity against HIV-1 PSV

The antiviral activities of the graphene-based NCs were evaluated by monitoring the infection of HeLa and THP-1 cells with an HIV-1-based PSV. This model is widely used to study the early phase of viral infection, from cell entry until the integration of the viral genome into host cell DNA. The PSV used

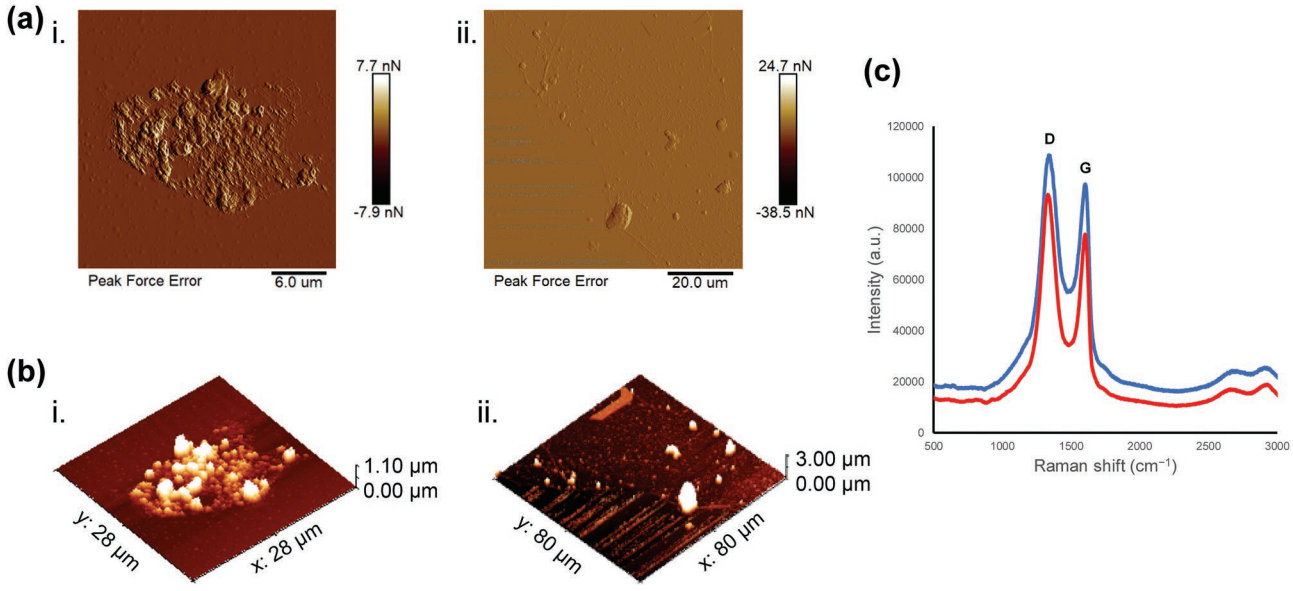

Figure 2. Characterization of single-layer rGO-Ag surfaces. a) 2D AFM images of rGO-Ag_L (i) and rGO-Ag_H (ii), b) 3D AFM images of rGO-Ag_L (i) and rGO-Ag_H (ii) showing the single-layer morphology and thickness, and c) Raman spectra of rGO-Ag_L and rGO-Ag_H showing the reduction state of rGO.

© 2022 The Authors. Advanced Materials Interfaces published by Wiley-VCH GmbH

21967350, 2023, 6, Downloaded from https://onlinelibrary.wiley.com/doi/10.1002/admi.202201996 by Technical University In Brno, Wiley Online Library on [04/08/2023]. See the Terms and Conditions (https://onlinelibrary.wiley.com/terms-and-conditions) on Wiley Online Library for rules of use; OA articles are governed by the applicable Creative Commons License

Table 1. Physicochemical characterization of the synthesized rGO-Ag samples.

Parameter	Method	rGO-Ag_L	rGO-Ag_H
Surface area [μm^2]	SEM	0.005–4.700, avg. 0.18	0.03–11.70, avg. 3.70
Thickness [μm]	AFM	0.04–1.11	0.04–0.37
Degree of defects I_D/I_G	Raman	1.11	1.20
Surface charge [mV]	Zeta potential	−42.9	−81.4
C sp^2 (%)	XPS	45.20	47.89
C−OH, C−O−C and C=O in C 1s region [%]	XPS	43.89, 9.92, 0.00	41.48, 9.68, 0.00
C=O, C−OH, H_2O in O 1s region [%]	XPS	16.75, 83.25, 0.00	14.84, 85.16, 0.00
Ag ($3d_{3/2}$) and Ag ($3d_{5/2}$) in Ag 3d region [%]	XPS	39.98, 60.02	39.98, 60.02

in this study was non-replicative since the viral genome was replaced by luciferase (PSV/luc)- or eGFP (PSV/gfp) genes, whose expression serves as a reporter of infection. To increase cell tropism, the HIV-1 envelope protein was replaced by a vesicular stomatitis virus glycoprotein (VSV-G) that ensured cell entry via endocytosis, independent of the presence of CD4 receptors on the cell surface.

To explore the impact of the graphene-based NCs on viral infectivity, the viral particles (PSV/luc) were incubated with a high concentration (100 μg mL^{-1}) of rGO-Ag for different time periods ranging from 5 to 90 min at room temperature. Following the incubation, the samples were centrifuged to remove the larger particles and aggregates, and the PSV-containing supernatants were deposited on the cells. 24 h post-infection (h.p.i.), the cells were lysed, and luciferase expression was measured. As shown in **Figure 4**a, the luciferase assay revealed that virus infectivity was significantly reduced in contact with rGO-Ag. This effect increased with time and reached a plateau at 90 min of PSV/rGO-Ag contact. Therefore, 90 min of incubation was performed in further experiments.

Next, we evaluated the dependence of infection inhibition on the rGO-Ag concentration. For this, HIV-1 PSV particles (PSV/luc) were incubated with increasing concentrations of rGO-Ag ranging from 1 to 2000 μg mL^{-1} for 90 min, followed by centrifugation and supernatant deposition on HeLa cells. Infection was measured 24 h.p.i. by luciferase activity. As shown in Figure 4b,c, the PSV infectivity was reduced by 50% (IC_{50}) when exposed to 48 μg mL^{-1} of rGO-Ag (based on the dry weight of the material), which corresponds to 22 μg mL^{-1} of Ag content. PSV incubation with 100 μg mL^{-1} rGO-Ag decreased the viral infectivity to less than 10%. The reduction state of rGO-Ag did not influence the observed virucidal effect, as rGO-Ag_L and rGO-Ag_H showed similar inhibitory activities (Figure S4, Supporting Information). rGO-Ag_L was selected for further study and is henceforth referred to as rGO-Ag.

The virucidal activity of rGO-Ag was then compared to that of Ag NPs and GO sheets used separately (Figure 4b,c). As shown in Figure 4b, the Ag NPs showed weak antiviral activity, reducing infection by only 30% even at very high concentrations. In contrast, PSV incubation with GO resulted in a significant reduction in infectivity with an IC_{50} value of 210 μg mL^{-1} (Figure 4c). The comparison of the inhibition caused by GO and Ag NPs separately

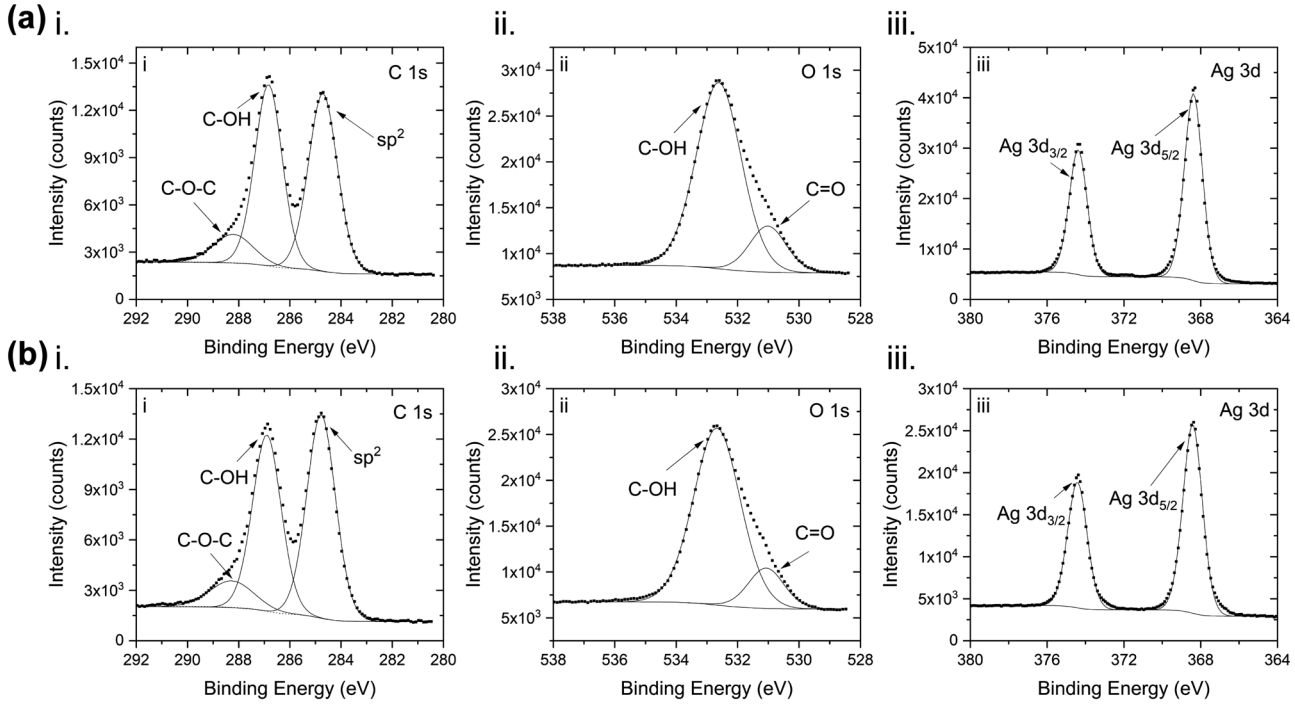

Figure 3. High-resolution XPS spectra of different rGO-Ag NC samples fitted with CasaXPS software (version 2.3.22) showing surface characteristics and bond structures. C 1s, O 1s, and Ag 3d region peaks of rGO-Ag_L (a) and rGO-Ag_H (b). The peak values indicate the type of covalent bonds present in the rGO-Ag samples.

© 2022 The Authors. Advanced Materials Interfaces published by Wiley-VCH GmbH

21967350, 2023, 6, Downloaded from https://onlinelibrary.wiley.com/doi/10.1002/admi.202201996 by Technical University In Brno, Wiley Online Library on [04/08/2023]. See the Terms and Conditions (https://onlinelibrary.wiley.com/terms-and-conditions) on Wiley Online Library for rules of use; OA articles are governed by the applicable Creative Commons License

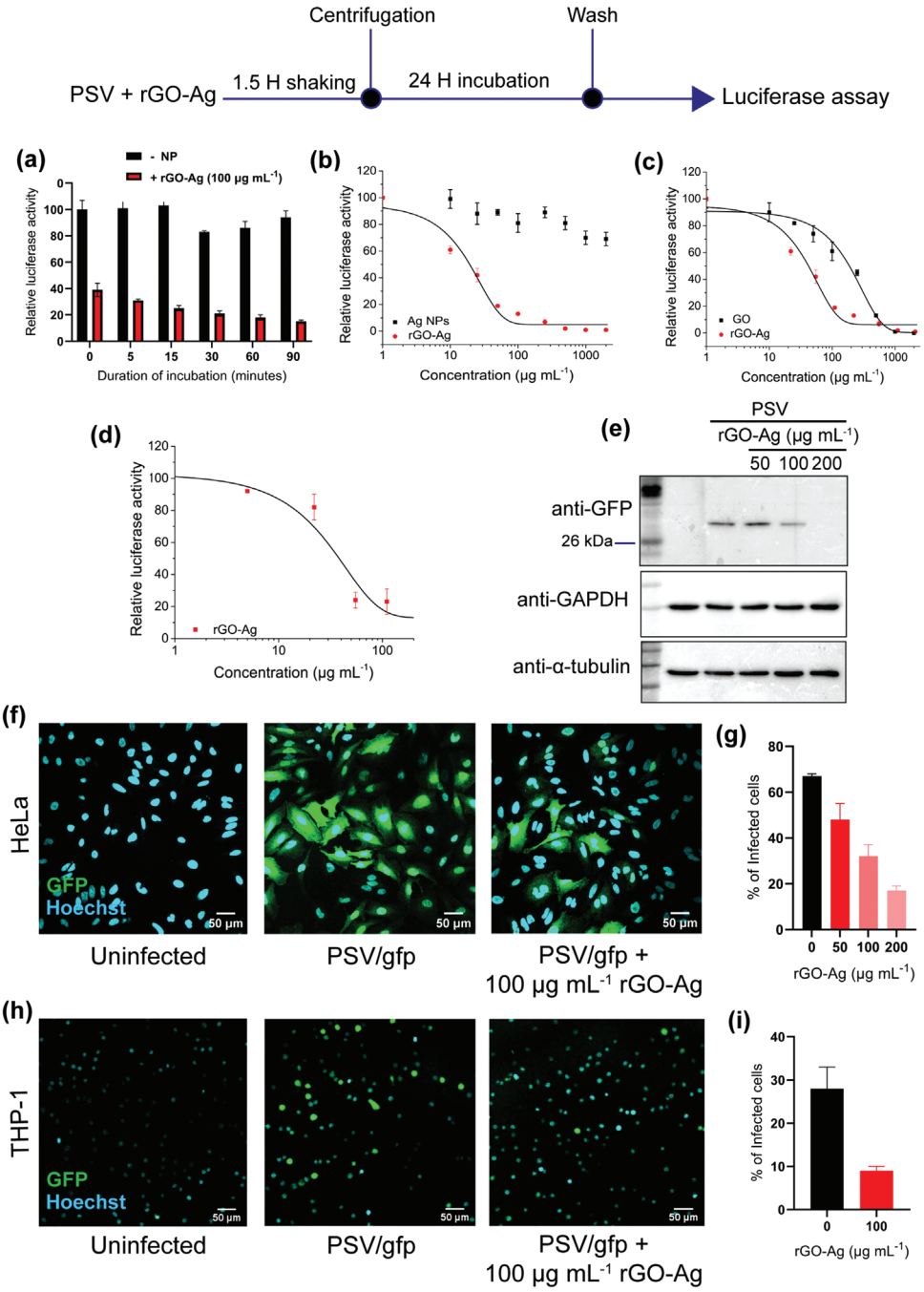

Figure 4. Virucidal effect of rGO-Ag NCs on HIV-1 PSV infection in HeLa and THP-1 cells. a) Time dependence of the virucidal effect of 100 µg mL^{-1} rGO-Ag NCs. b) Inhibition of viral infection in HeLa cells by exposure to rGO-Ag NCs and Ag NPs. The concentration refers to the silver concentration in both types of nanomaterials. c) Inhibition of viral infection in HeLa cells by exposure to GO and rGO-Ag NCs. The concentration refers to the total weight of the nanomaterial. d) Inhibition of viral infection in THP-1 cells by exposure to rGO-Ag NCs. e) Detection of eGFP in the cell lysate after incubation with PSV/gfp pre-incubated with increasing concentrations of rGO-Ag. f) Fluorescence images of HeLa cells infected with HIV-1 PSV/gfp and g) fraction of HeLa cells expressing eGFP 24 h.p.i,.mean value ± STD, n = 2000 cells were analyzed for each condition. h) Fluorescence images of THP-1 cells infected with HIV-1 PSV/gfp and i) fraction of THP-1 cells expressing eGFP, mean value ± STD, n = 2000 cells were analyzed for each condition.

with the inhibition caused by rGO-Ag indicated a clear synergistic effect. To investigate the dependence of the antiviral effect of rGO-Ag on the cell line, the same experiments were repeated with THP-1 cells. As shown in Figure 4d, a very similar infection inhibition was observed in THP-1 cells, with an IC_{50} = 43 µg mL^{-1}.

Next, the effect of rGO-Ag on viral infectivity was tested using PSV/gfp. Supernatant samples containing this PSV were prepared by the abovementioned method in the presence of increasing amounts of rGO-Ag and used to infect HeLa cells and THP-1 cells. At 24 h.p.i., the cells were either harvested for

© 2022 The Authors. Advanced Materials Interfaces published by Wiley-VCH GmbH

21967350, 2023, 6, Downloaded from https://onlinelibrary.wiley.com/doi/10.1002/admi.202201996 by Technical University In Brno, Wiley Online Library on [04/08/2023]. See the Terms and Conditions (https://onlinelibrary.wiley.com/terms-and-conditions) on Wiley Online Library for rules of use; OA articles are governed by the applicable Creative Commons License

whole-cell extract preparation or processed for fixation prior to imaging or flow cytometry. The fluorescence-activated cell sorting (FACS) analysis of the THP-1 cells showed a significant decrease in the median GFP fluorescence intensity in cells treated with rGO-Ag compared to that in untreated cells. As the cell population with a significant fluorescent signal was relatively low (≈10%) (Figure S5, Supporting Information), the samples were observed by fluorescence microscopy, which ensures increased sensitivity compared to FACS. As demonstrated in Figure 4f–h, both the number of GPF-expressing cells and the eGFP content in the cell lysate were significantly reduced in samples treated with rGO-Ag. Whole-cell lysate immunoblotting revealed that the GFP expression was less than 50% with exposure to 100 μg mL^{-1} of rGO-Ag compared to the control, and no expression was observed with 200 μg mL^{-1} of NCs (Figure 4e). A similar result was observed when GFP expression was studied by fluorescence microscopy. The imaging of multiple slides revealed that at 24 h.p.i., ≈70% of HeLa cells were infected and expressed GFP (Figure 4f,g). Exposing PSV particles to increasing concentrations of rGO-Ag reduced the fraction of eGFP-expressing cells to less than 20% (for 200 μg mL^{-1} rGO-Ag), indicating a significant loss of viral infectivity. In THP-1 cells infected with PSV/gfp for 30 h, ≈30% of the cells expressed GFP in the control samples, whereas less than 10% of cells were infected (Figure 4h,i) when the PSV particles were exposed to 100 μg mL^{-1} of rGO-Ag. Altogether, our data showed that PSV incubation with rGO-Ag resulted in the potent inhibition of viral infectivity.

2.3. Effects of rGO-Ag NCs on Cellular Viability

Since the viral infectivity of the HIV-1 PSV particles was measured by the expression of reporter genes, it was necessary to verify that the infected cells were perfectly viable and that the observed decrease in Luc and GFP levels was not caused by cytotoxic effects. During sample preparation, the PSV was incubated with the rGO-Ag (rGO-Ag_p). Then, the samples were centrifuged, and the PSV-containing supernatants (rGO-Ag_s) were deposited on the cells. The initial sample and the supernatant shown in **Figure 5**a clearly indicate that the majority

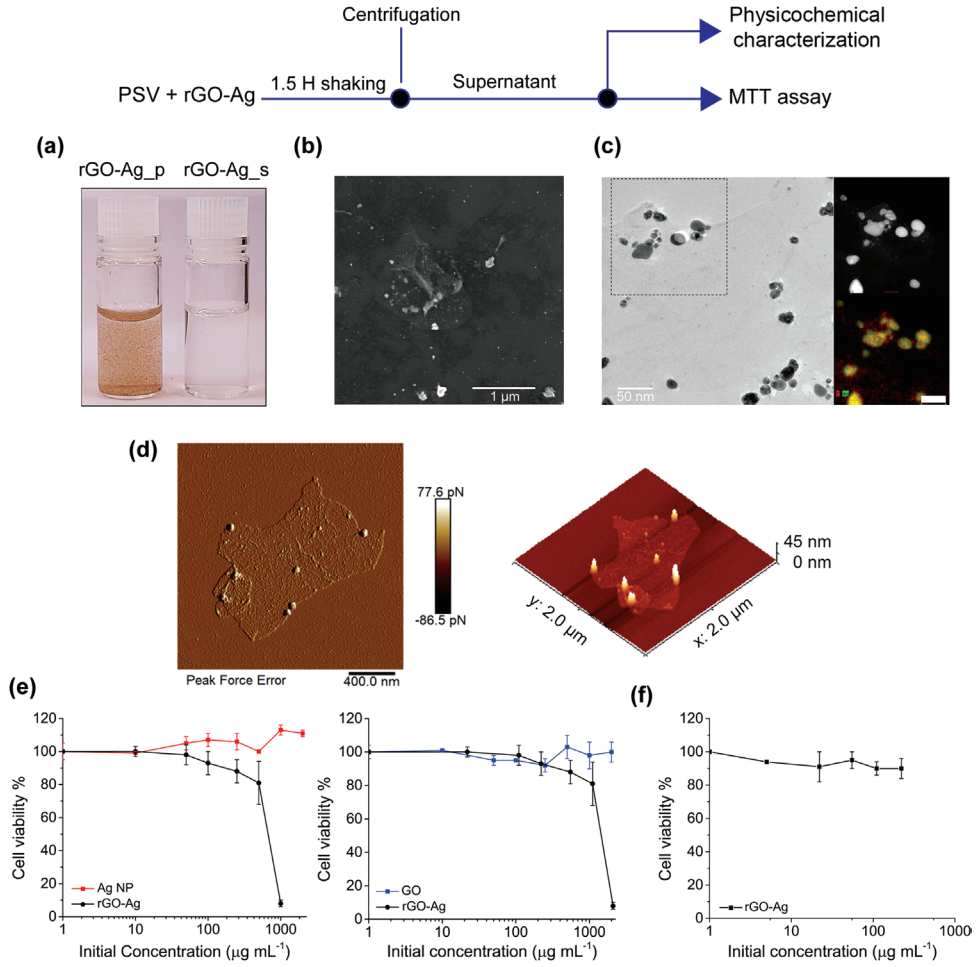

Figure 5. Characterization of the rGO-Ag in the supernatant and cellular toxicity analysis. a) Visual comparison of rGO-Ag whole particles (rGO-Ag_p) and supernatant (rGO-Ag_s) in PBS at 100 μg mL^{-1}, b) SEM image showing the sheet-like morphology of rGO and the Ag NP distribution on the surface, c) TEM, STEM, and EDS mapping showing the nanoscale Ag NP distribution on the rGO sheet, d) AFM analysis of rGO-Ag in the supernatant depicting the single-layer topography of the nanomaterial. Cell viability of HeLa (e) and THP-1 (f) cells after incubation with the supernatants containing PSV/luc and increasing concentrations of rGO-Ag NCs.

© 2022 The Authors. Advanced Materials Interfaces published by Wiley-VCH GmbH

21967350, 2023, 6, Downloaded from https://onlinelibrary.wiley.com/doi/10.1002/admi.202201996 by Technical University In Brno, Wiley Online Library on [04/08/2023]. See the Terms and Conditions (https://onlinelibrary.wiley.com/terms-and-conditions) on Wiley Online Library for rules of use; OA articles are governed by the applicable Creative Commons License

21967350, 2023, 6, Downloaded from https://onlinelibrary.wiley.com/doi/10.1002/admi.202201996 by Technical University In Brno, Wiley Online Library on [04/08/2023]. See the Terms and Conditions (https://onlinelibrary.wiley.com/terms-and-conditions) on Wiley Online Library for rules of use; OA articles are governed by the applicable Creative Commons License

of rGO-Ag were pelleted and removed during centrifugation. Therefore, we first analyzed the PSV-containing supernatants used for infections. AAS analysis confirmed that the supernatant contained ≈5% of the initially present rGO-Ag (data not shown). The size of rGO-Ag_s was investigated by SEM and TEM coupled with STEM-EDS (Figure 5b,c) and the surface topography was visualized by AFM (Figure 5d). These analyses revealed that the NCs in the supernatants were significantly smaller than the originally synthesized NCs shown in Figure 1. The NC size distribution according to the measured surface area is given in Figure S6, Supporting Information. In addition, TEM/STEM-EDS analysis confirmed the presence of Ag NPs on the nanosheet surfaces. These observations confirmed that the PSV-containing supernatants used for infection contained nano to micrometer-sized rGO-Ag sheets.

To determine the potential cytotoxicity of these rGO-Ag sheets, the viability of HeLa and THP-1 monocytic cells was measured by MTT assay after 24 h of incubation with PSV particles and NC-containing supernatants. The cells were cultured and infected under the same conditions as the previous infectivity experiments. Briefly, the PSV particles (PSV/luc) were incubated in the presence of various concentrations of rGO-Ag, GO, and Ag NPs for 90 min, followed by centrifugation, and the supernatants were deposited on the cells for 24 h. Afterward, MTT assays were performed to assess cell viability. As shown in Figure 5e, the relative survival rate of HeLa cells when exposed to all types of NCs was greater than 80%, suggesting good biocompatibility. The THP-1 cells, which are more sensitive to culture conditions, showed higher cell death when exposed to supernatants containing high NC concentrations (initial concentration of 200 μg mL^{-1}), whereas the relative cell viability was greater than 80% at 100 μg mL^{-1} of rGO-Ag NCs (Figure 5f). Since it was experimentally difficult to measure the Ag NPs and GO concentrations in the supernatant, to avoid any bias, all curves in Figure 5e,f are plotted with initial sample concentrations. Moreover, the cellular morphology did not change in our experiments. These observations clearly indicate that in both cell lines, infection inhibition was observed under noncytotoxic conditions. Therefore, the decrease in luciferase and GFP expression did not result from cell death but reflected a real suppression of viral infectivity.

2.4. Mechanism of the rGO-Ag Antiviral Activity

To understand the mechanism underlying the antiviral activity of the rGO-Ag NCs, we investigated a few possible hypotheses. GO sheets naturally bind biomolecules through different surface groups that establish covalent or electrostatic interactions.[41] Although the chemical reduction of GO removes most oxygen-containing groups from the surface, a significant amount of oxygen-rich functional groups is left to bind biomolecules, as seen from the XPS analysis (Figure 3). Moreover, Ag NPs can bind to the −SH groups of the VSV-G envelope glycoproteins. All these interactions may facilitate binding between the NCs and viral particles during incubation. We therefore hypothesized that a significant fraction of the PSV particles might be bound and pelleted together with the rGO-Ag during the centrifugation step. Consequently, the observed decrease in Luc expression simply reflects this loss of PSV particles. In addition, the interactions of GO and GO-Ag with microorganisms or viruses were previously shown to rupture their membranes, leading to the release of their internal content. Similar rGO-Ag-induced rupture of the pseudoviral particles could possibly cause the decrease in infection observed in our experiments.

To check the possible mechanical disruption or the removal of the viral particles from the samples by binding to rGO-Ag, we examined the total supernatant PSV content. The viral particles were incubated for 90 min with 50, 100, and 200 μg mL^{-1} rGO-Ag or left untreated. The samples were centrifuged, and the total p24 protein amount in the supernatant was measured by ELISA. The p24 protein is a component of the HIV-1 capsid structure that protects the viral core. As indicated in **Figure 6**a, exposure to rGO-Ag and subsequent centrifugation caused only a limited loss of p24 protein. When incubated with 200 μg mL^{-1} of rGO-Ag (conditions that lead to the complete loss of infectivity), the supernatant still contained ≈77% of the initially present p24. However, the total p24 content only provided information about the presence of capsid protein in the sample but did not distinguish between mature capsid in intact viral particles from capsid protein that might be released upon disruption of the viral core or from the capsid domain of non-processed Gag polyprotein. To check for the presence of intact PSV particles in the supernatant, ultracentrifugation was performed to separate the complete PSV particles from the potentially released viral proteins. The pellet was lysed and immunoblotted with an antibody against the HIV-1 integrase protein. Figure 6b shows that there was no significant reduction in the amount of integrase in the rGO-Ag-exposed samples compared to control. These results clearly showed the presence of mature PSV particles in the supernatant, highlighting that exposure to rGO-Ag did not alter the viral core or pull down viral particles during centrifugation.

To further evaluate the effect of rGO-Ag on viral particles, the morphology of the PSVs was observed by SEM. PSV/luc were treated with 100 μg mL^{-1} rGO-Ag for 90 min. The samples were then centrifuged, and the supernatants were deposited on collagen-coated coverslips. As shown in Figure 6c, the spherical shape of the viral particles was unaltered upon exposure to the NCs. Changes in the PSV particle size were also negligible. rGO-Ag-treated viral particles were also imaged at the surface of HeLa cells after 1 h of incubation at 4 °C. At this low temperature, the viruses can attach to the surface receptors of the host cells, but their cellular entry via endocytosis is inhibited. The SEM images in Figure 6c show that upon exposure to rGO-Ag, the viral particles were still able to attach to the cells, and no significant difference in their number or morphology was observed. However, since sample preparation for SEM requires numerous washing steps, it is impossible to estimate the fraction of PSV particles lost during sample processing and hence to conclude about any potential decrease in the number of PSVs attached on the cell surface. In any case, the observed viral particles in the rGO-Ag treated samples were not significantly affected compared to non-treated ones and were still bound to the cell surface. Altogether, our data do not evidence any significant binding between rGO-Ag NCs and viral particles, refuting the hypothesis that a loss of infectious viral particles from the

© 2022 The Authors. Advanced Materials Interfaces published by Wiley-VCH GmbH

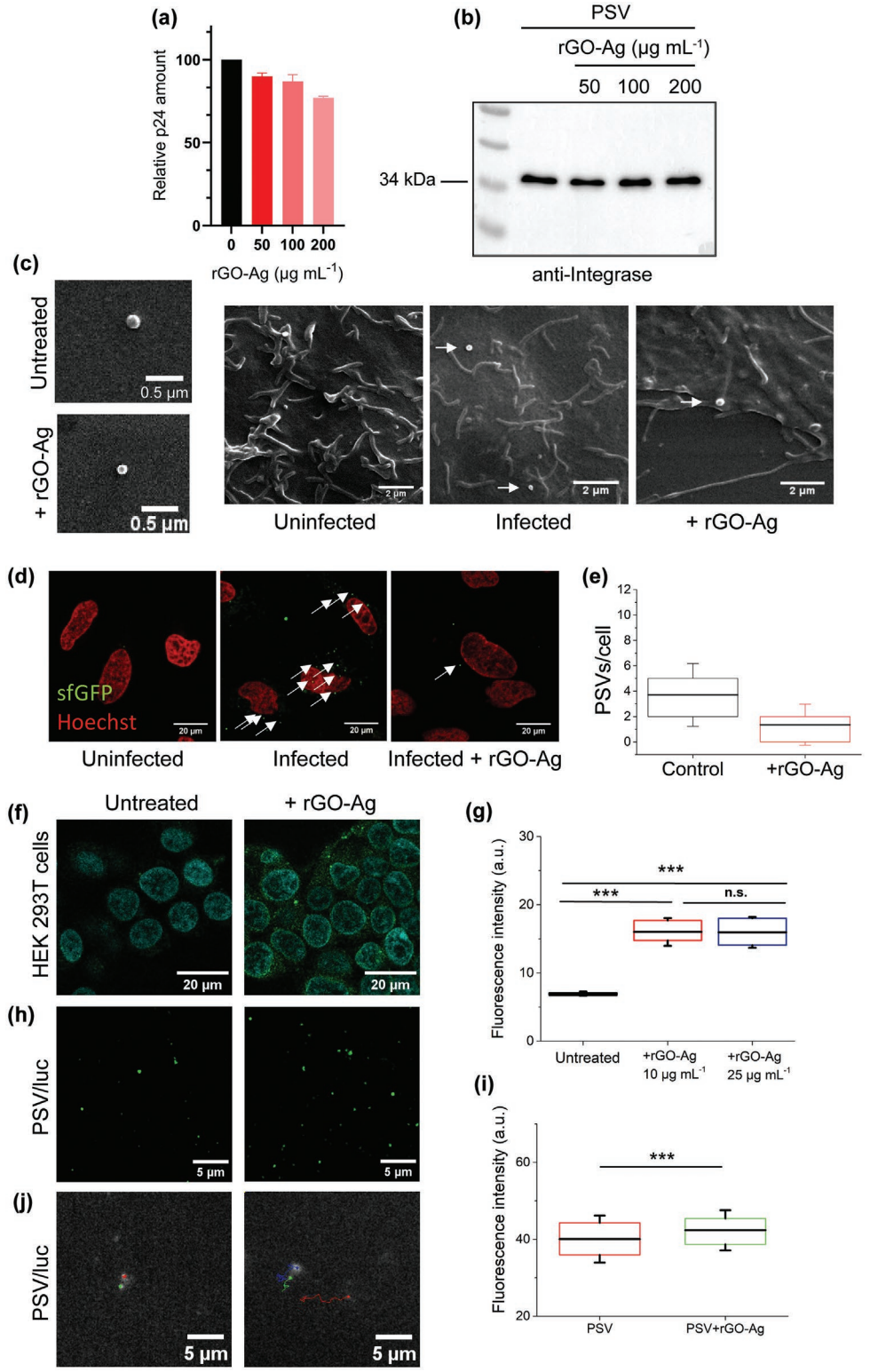

Figure 6. Mechanism of the antiviral effect of rGO-Ag NCs against HIV-1 PSV. a) Quantification of p24 viral antigen concentration in the supernatants by ELISA. b) Immunoblot analysis of integrase protein in the supernatants of PSV treated with increasing concentrations of rGO-Ag. c) SEM images of PSVs incubated in the presence of 100 μg mL^{-1} rGO-Ag or left untreated. d) Confocal images of HeLa cells infected with IN-sfGFP-containing HIV-1 PSV (PSV/IN-gfp) for 2 h. Cell nuclei were stained with Hoechst. White arrows indicate intracellular fluorescent PSV particles. e) Quantification of PSV/IN-gfp particles detected in the middle planes of the cells. The fluorescent spots larger than twice the resolution limit (500 nm) that correspond to aggregates were excluded from the analyzed data; $n = 85$ for each condition, the box represents 25–75% of the data, the whisker represents the SD, and the line shows the mean value. f–i) HEK 293T cells or PSV/luc were treated with various concentrations of rGO-Ag or left untreated and

© 2022 The Authors. Advanced Materials Interfaces published by Wiley-VCH GmbH

21967350, 2023, 6, Downloaded from https://onlinelibrary.wiley.com/doi/10.1002/admi.202201996 by Technical University In Brno, Wiley Online Library on [04/08/2023]. See the Terms and Conditions (https://onlinelibrary.wiley.com/terms-and-conditions) on Wiley Online Library for rules of use; OA articles are governed by the applicable Creative Commons License

supernatant or the mechanical disruption of the virus by NCs might inhibit viral infection.

Next, we used fluorescent HIV-1 PSV particles (PSV/IN-sfGFP)[42] to examine their cellular entry by fluorescence microscopy. PSV particles were treated with 100 μg mL^{-1} of rGO-Ag or left untreated. The samples were centrifuged, and HeLa cells were infected with the collected supernatant for 2 h to allow the viral particles to enter the cells. The samples were fixed and imaged by confocal microscopy. PSVs expressing IN-superfolder green fluorescent protein (sfGFP) were detected as fluorescent spots in the cytoplasm of the infected cells. The number of detected viral particles was counted in the middle plane of the cells to avoid counting the PSVs at the cell surface. As shown in Figure 6d,e, HeLa cells infected with nontreated PSVs contained on average 3.8 cytoplasmic spots, whereas only 1.25 viral particles were detected when the PSVs were preincubated with rGO-Ag (Figure 6e). These data suggest that rGO-Ag effectively reduces viral entry into host cells.

It has been previously reported that graphene-based nanomaterials show oxidative activity and may trigger reactive oxygen species (ROS) generation and lipid peroxidation in mammalian cells.[27,43] Therefore, the NC-induced alteration of the PSV lipid envelope can potentially affect the binding of PSV to the host cell surface and its cell entry. To test this hypothesis, the level of lipid peroxidation resulting from incubation with rGO-Ag NCs was measured by Liperfluo labeling. Liperfuo dye emits fluorescence specifically in the presence of lipid peroxides. These experiments were first performed on HEK 293T cells since our model PSV particles are enveloped in a lipid membrane that is recovered from the plasma membrane of HEK 293T cells during viral budding. Cells were incubated with 100 μg mL^{-1} rGO-Ag for 3 h, followed by washing and labeling with Liperfluo dye. As shown in the confocal images and corresponding plot in Figure 6f,g, the presence of rGO-Ag led to an increase in Liperfluo fluorescence in the cells, indicating that rGO-Ag induced the lipid peroxidation of their membranes. Similarly, HIV-1 PSV particles were incubated with rGO-Ag for 90 min, followed by ultracentrifugation and staining with Liperfluo dye. The PSV particles were then loaded into an Ibidi channel slide and imaged with confocal and epifluorescence microscopes. The mean Liperfluo intensity of individual PSV particles showed a significant increase for the rGO-Ag treated sample (Figure 6h). Interestingly, we also observed very different motility of treated and nontreated viral particles. In the nontreated samples, numerous viral particles were attached to the glass coverslip surface, while in the rGO-Ag treated samples, the majority of the viral particles diffused in the buffer, and only a few of them were attached. Figure 6j (and Videos S1 and S2, Supporting Information) represents the trajectories of individual viral particles in the control and rGO-Ag treated samples. Altogether, these results indicate that rGO-Ag induces lipid peroxidation and modifies the physicochemical properties of the viral external membrane.

In conclusion, our data suggest that rGO-Ag does not disrupt or remove PSV particles from the samples during the centrifugation step. However, they cause lipid peroxidation, which could alter the properties of the viral and cellular membranes, preventing viral entry.

2.5. Cellular Uptake of rGO-Ag and Stimulation of the Cell Proinflammatory Response

It was previously reported that cell membrane interaction and GO-Ag internalization can stimulate cell signaling, which may lead to the inhibition of the viral infection.[17,44] To explore this possible contribution to our observations, we examined the cellular uptake of rGO-Ag by HeLa cells. Since rGO-Ag nanomaterials emit fluorescence,[45] it was possible to visualize them inside the cells by confocal microscopy. The supernatant of rGO-Ag was prepared as mentioned above and incubated with cells for 3 or 24 h. **Figure 7**a reveals the presence of fluorescent spots in the rGO-Ag treated cells, while no fluorescence was detected in the control sample. As shown in the higher-magnification image, rGO-Ag was clearly present in the cell cytoplasm. These observations indicate that rGO-Ag is efficiently taken up by the cells and can be detected in the cell cytoplasm after 3 h of incubation.

Next, we examined whether the preincubation of rGO-Ag with cells had any effect on viral infection. HeLa and THP-1 cells were exposed to supernatants containing different concentrations of rGO-Ag for 3 and 24 h followed by extensive washing to remove all unbound nanoparticles. The cells were then infected with PSV/luc, and their luciferase activity was measured after 24 h. As demonstrated in Figure 7b, a short (3 h) preincubation of HeLa cells with rGO-Ag did not affect viral infection. In contrast, when cells were incubated with rGO-Ag for 24 h prior to infection, their luciferase activity was reduced to 68% and 39% for the HeLa and THP-1 cells, respectively (Figure 7c,d).

Since the PSV was not in contact with the rGO-Ag materials before infection, we suggest that these results show an alternate inhibitory effect of rGO-Ag that occurs most likely during the intracellular steps of the viral cycle.

As mentioned earlier, one of the possible mechanisms responsible for rGO-Ag-induced antiviral activity could be related to innate immunity activation. We, therefore, studied the effect of rGO-Ag on the cellular inflammatory response at the transcriptional level. THP-1 and HeLa cells were incubated with supernatants containing rGO-Ag (samples initially containing 50 μg mL^{-1}) for 24 h. This incubation was followed by total RNA extraction and two-step quantitative reverse transcription–polymerase chain reaction (qRT–PCR) assays. We found that rGO-Ag strongly stimulated the production of proinflammatory cytokine mRNAs, such as TNF-α, IL-8, IL-1β, and IL-6, in the THP-1 and HeLa cells. As demonstrated in

stained with Liperfluo dye (final concentration 1 μmol L^{-1}) in serum-free media. f) Confocal images of HEK 293T cells stained with Liperfluo dye. g) Representative graph of the mean fluorescence intensities in the cell area; $n = 70$ for each condition, the box represents 25–75% of the data, and the whisker represents the SD. h) Confocal images of the PSV/luc stained with Liperfluo dye. i) Mean fluorescence intensities of fluorescent spots corresponding to individual viruses; $n = 400$ for each condition, the box represents 25–75% of the data, the whisker represents the standard deviation (SD), and $^{***}p < 0.001$. j) Trajectories of rGO-Ag-treated or untreated PSV/luc.

© 2022 The Authors. Advanced Materials Interfaces published by Wiley-VCH GmbH

21967350, 2023, 6, Downloaded from https://onlinelibrary.wiley.com/doi/10.1002/admi.202201996 by Technical University In Brno, Wiley Online Library on [04/08/2023]. See the Terms and Conditions (https://onlinelibrary.wiley.com/terms-and-conditions) on Wiley Online Library for rules of use; OA articles are governed by the applicable Creative Commons License

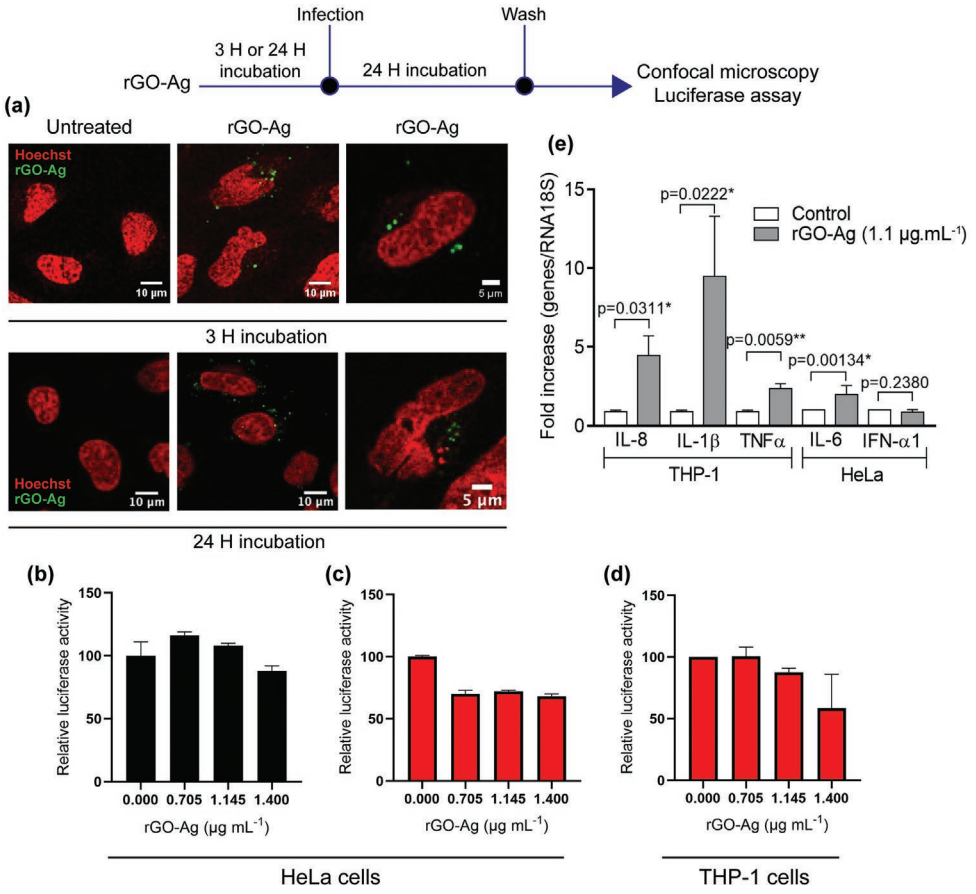

Figure 7. Cellular uptake of rGO-Ag at different incubation times and its effect on PSV infection. a) Confocal images of HeLa cells incubated for 3 and 24 h with rGO-Ag, b,c) HeLa cells that were in contact with rGO-Ag for 3 h (b) and 24 h (c) and then washed. The samples were infected with PSV/luc, and their luciferase activity was quantified after 24 h of infection. Plotted values represent the mean value and the standard deviation of two independent experiments, each performed in triplicate. d) THP-1 cells that were in contact with rGO-Ag for 24 h and then washed. The samples were infected with PSV/luc, and their luciferase activity was quantified after 24 h of infection. e) Effect of rGO-Ag on the transcription of proinflammatory genes in THP-1 and HeLa cells by qRT–PCR assay (n = 8 and 4 for THP-1 and HeLa cells, respectively). Data represent the mean ± S_E. After Student analysis, $p < 0.05$ was considered significant.

Figure 7e, the transcription of IL-8, IL-1β, TNF-α, and IL-6 was 4.46, 9.46, 2.82, and 1.50 times higher, respectively, in the group of cells treated with the rGO-Ag NCs compared to that in the control group. The production of IFN-α in HeLa cells in response to NC treatment was also tested, but no significant change in mRNA expression was observed. These data suggest that rGO-Ag could stimulate proinflammatory responses to indirectly inhibit viral infection.

3. Discussion

Graphene-based materials are attracting increasing interest in biomedical applications. 2D graphene-derivatives have shown true potential and advantages over other related carbon nanomaterials for use in photonics and biomedicine. Their antimicrobial activity together with their biocompatibility and low toxicity make them highly promising for the prevention and limitation of the spread of microbial infections. However, the antiviral effects of graphene-based materials are not fully understood and represent a challenge.

Here, we used a chemical reduction method to synthesize rGO NCs decorated with Ag NPs. The successful preparation of the single-layer 2D nanomaterial was confirmed by AFM analysis. The thickness of the GO sheets depends on the number of layers and the type of attached functional groups. The average thickness of one GO sheet is ≈0.93 nm.[46] The functional groups form a layer above the sheet and add a thickness of ≈0.78 nm.[46,47] Epoxy groups protrude above the carbon lattice, adding a thickness of ≈0.19 nm, while hydroxyl groups over the carbon lattice add ≈0.22 nm. These earlier reported measurements are in accordance with the results of the XPS analysis that identified functional groups in the synthesized composites.

Sodium borohydride was used as a reducing agent, which exhibits stronger reducing properties in comparison with milder reducing agents, for example, glucose[48] or citrate,[49] used in contemporary studies. The efficient reduction of GO was confirmed by XPS and Raman spectroscopy. According to the XPS analysis, the number of sp^2 hybridized carbon atoms slightly increased, and the ratio between the intensities of the D and G peaks in Raman spectroscopy indicated a further increase in sp^2 hybridized carbon atoms. EM images

© 2022 The Authors. Advanced Materials Interfaces published by Wiley-VCH GmbH

21967350, 2023, 6, Downloaded from https://onlinelibrary.wiley.com/doi/10.1002/admi.202201996 by Technical University In Brno, Wiley Online Library on [04/08/2023]. See the Terms and Conditions (https://onlinelibrary.wiley.com/terms-and-conditions) on Wiley Online Library for rules of use; OA articles are governed by the applicable Creative Commons License

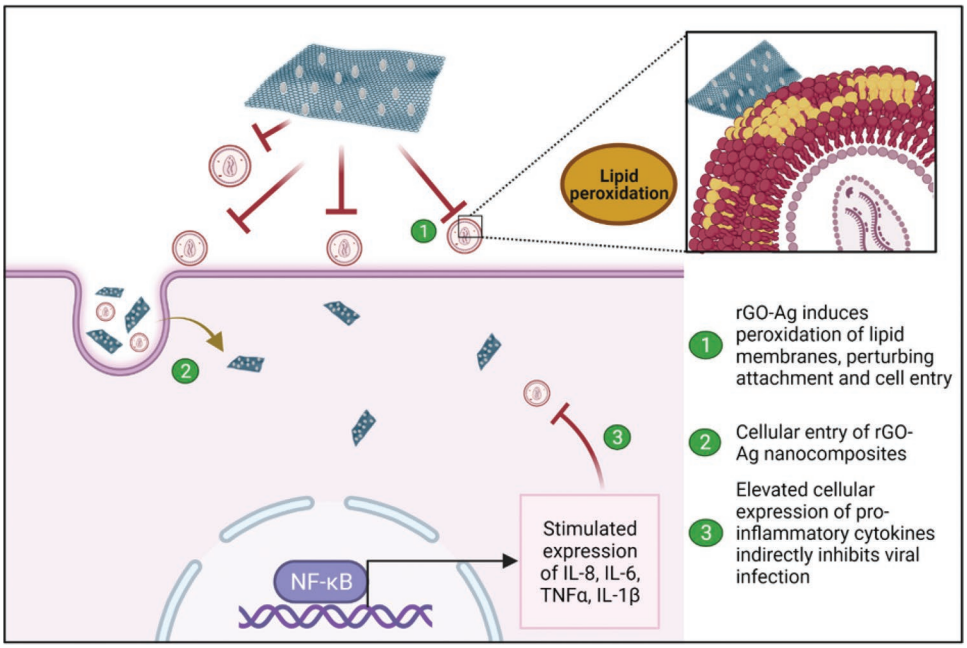

Scheme 1. Suggested mechanisms of rGO-Ag antiviral activity.

demonstrated that Ag NPs were uniformly distributed on the rGO sheets. Due to its 2D sheet-like structure, rGO provided a sufficient stabilizing effect to protect Ag NPs against aggregation in biological media.

The antiviral activity of the synthesized rGO-Ag against HIV-1-based PSV was evaluated in HeLa and THP-1 cell lines. Complementary biochemical and fluorescence microscopy-based approaches were employed to follow the early steps of viral infection and quantify the rGO-Ag-induced alterations at the single-virus level. Our results revealed that the physical contact of PSV particles with rGO-Ag significantly reduced their infectivity and that this effect was stronger in comparison to that of GO sheets or Ag NPs alone. This synergistic effect of Ag NPs with GO sheets is in agreement with observations reported by Du et al., who studied the antiviral activity of GO-Ag NCs against PRRSV.[17] Interestingly, Ag NPs showed only a slight virucidal effect in our experiments, which indicates that the rGO sheets play a key role, probably by limiting the aggregation of Ag NPs and hence facilitating the physical interactions with the viral particles. It is noteworthy that the Ag NPs used in this study are bigger (15 nm) compared to 1–10 nm sized Ag NPs that were shown previously to efficiently inhibit HIV-1 infection.[50] Indeed, the size and shape of Ag NPs play an important role in determining their biological effect.[51] Smaller Ag NPs (≈5–20 nm) were reported to be more toxic[52] to mammalian cells and bacteria in comparison to bigger NPs (≈50 nm).[53–55] Therefore, the mild antiviral effect of Ag NPs observed in this study may be related to the size of the NPs, and the antiviral activity of rGO-Ag sheets could be possibly enhanced by using smaller Ag NPs.

Next, we focused on rGO-Ag NCs and evaluated various interactions to explain the observed antiviral effects. Based on our experiments, we suggest that the observed infection inhibition results from a combination of lipid peroxidation that alters the properties of the viral envelope and the induction of the cell's innate immunity response (see **Scheme 1**).

First, we examined the possibility of rGO-Ag binding to PSV, leading to the removal of viral particles from the samples or to their mechanical disruption, as was previously reported for viruses and bacteria.[14,16,20,26] Interestingly, our data showed that the binding of PSV particles to the nanosheets was limited. Moreover, the samples treated with rGO-Ag had a morphology similar to that of the nontreated samples, and the viral core remained intact. Since rGO-Ag-treated samples exhibited a decreased number of intracellular viral particles, we concluded that rGO-Ag induced a loss of virus infectivity, most likely resulting from a mild nondestructive perturbation of the PSV surface, which in turn impeded viral entry.

GO and rGO have been previously shown to induce lipid peroxidation of the cell plasma membrane[43] and alterations in mitochondrial functions.[56] Since lipid peroxidation impacts the biophysical properties of membranes, (e.g., viscosity and phase behavior) and protein mobility within the bilayer,[57,58] we speculate that similar modifications of the pseudoviral and cellular membranes might be responsible for the infectivity loss. In line, rGO-Ag induced the lipid peroxidation of the HEK 293T membranes and the less pronounced, although significant, peroxidation of the viral lipid membrane. In addition, the attachment of the PSV particles to the glass surface significantly decreased upon rGO-Ag treatment, confirming the modification of the PSV surface properties. The cell entry of PSV particles occurs through phosphatidyl serine receptor binding[59] on the cell surface followed by endocytosis and pH-dependent release.[60] These steps require optimal fluidity and integrity of external membranes. Therefore, lipid peroxidation induced by rGO-Ag NCs impacted the membrane biophysical properties that might inhibit the cell entry of the PSV particles. HIV-1 PSV was used in this study as a model of enveloped viruses. It is

© 2022 The Authors. Advanced Materials Interfaces published by Wiley-VCH GmbH

21967350, 2023, 6, Downloaded from https://onlinelibrary.wiley.com/doi/10.1002/admi.202201996 by Technical University In Brno, Wiley Online Library on [04/08/2023]. See the Terms and Conditions (https://onlinelibrary.wiley.com/terms-and-conditions) on Wiley Online Library for rules of use; OA articles are governed by the applicable Creative Commons License

highly probable that rGO-Ag exhibits a similar inhibitory effect on other types of viruses protected by an envelope derived from the host cell such as Influenza (Orthomyxoviridae family) or Coronaviruses.

The first part of the study showed a clear virucidal effect exhibited by rGO-Ag. In the next step, we examined whether rGO-Ag might additionally inhibit infection by perturbing the cell, notably by influencing host cell signaling. The biological role of graphene derivatives depends greatly on their interactions with the plasma membrane and their ability to internalize efficiently. These interactions are significantly influenced by the physicochemical properties of the material and its shape, size, functional groups, and modifications (for a detailed review, see ref. [61]).

Our results confirmed that the rGO-Ag present in the supernatants was efficiently internalized by cells owing to the flexible property of the 2D structure. Moreover, the preincubation of cells with rGO-Ag for 24 h led to potent infection inhibition. These results indicate that rGO-Ag might impact cellular processes, which in turn inhibit the infection. The interplay between host immune signaling and graphene derivatives has been explored in the past. Several studies have reported that the cellular uptake of GO triggers cellular signaling pathways that are important for defense mechanisms.[17,62,63] Qu et al. showed that the interaction of GO with the TLR4 receptor stimulated the production of TNFα. Triggering the TLR4 signaling cascade stimulates the activation of the NF-κB pathway, which results in the increased expression of proinflammatory cytokines such as IL-1β. Similarly, several recent studies have shown that carbon nanomaterials, including GO, can trigger the activation of the NLRP3 inflammasome.[64,65] In line with reported observations, our results revealed that rGO-Ag induced proinflammatory genes in THP-1 monocytes and HeLa cells. The mRNA levels of proinflammatory cytokines, such as TNF-α, IL-8, IL-1β, and IL-6, were found to be increased compared to those of non-treated cells. Thus, cellular treatment with rGO-Ag NCs likely triggered the NF-κB pathway, inducing an immune response that inhibited HIV-1 PSV infection.

4. Conclusion

In this study, we demonstrated the potent antiviral activity of 2D rGO-Ag against HIV-1 PSV at a non-cytotoxic concentration. rGO-Ag was derived from graphite and Ag precursor in a facile synthesis route. AFM analysis showed a characteristic single-layer structure of synthesized nanomaterial with a surface decorated with Ag NPs. Using various biochemical and imaging approaches, we showed that the antiviral activity of the nanocomposite toward HIV-1 PSV was time- and dose-dependent. rGO-Ag showed a superior synergistic inhibitory effect compared to GO sheets or Ag nanoparticles alone. To deepen the understanding of the role of Ag NP in the antiviral activity of rGO-Ag nanocomposite, it would be interesting to further follow the impact of the size and/or shape of Ag NPs. Presented data showed that rGO-Ag-induced lipid peroxidation of the outer viral membrane led to changes in its biophysical properties. These data suggest that the physical interactions of rGO-Ag inactivated a significant population of viral particles impeding their cellular entry. In addition, the presented study showed that rGO-Ag was internalized by host cells and triggered the transcription of several pro-inflammatory genes, which probably contributed to an alternate mechanism of inhibition of viral infection. Altogether, this study demonstrates that reduced graphene-based materials represent interesting platforms for limiting the spread of infections caused by enveloped viruses and represent a high potential for the development of antimicrobial materials.

Future studies should be undertaken to deepen the understanding of the interactions of graphene derivatives with biological partners. Since these nanomaterials are efficiently internalized by cells, their impact on cell metabolism and gene expression is an important point to be clarified. Similarly, the consequences of graphene-induced oxidation and ROS production in the cells and tissues should be explored. The alteration of membrane biophysical properties, such as fluidity and lipid order, would be of importance due to their direct impact on the membrane trafficking, dynamics of membrane proteins, and triggering of intracellular signaling pathways.

5. Experimental Section

Chemicals: All chemicals used for syntheses were purchased from Sigma–Aldrich (St. Louis, MO, USA) unless otherwise stated. Demineralized water was produced using an Aqual 25 reverse osmosis apparatus (Aqual, Česká, Czech Republic) and further treated with Millipore System Inc. (Billerica, MA, USA) to obtain ultrapure water with a resistivity of 18.20 MΩ cm (at 25 °C). For determining Ag concentration, all solutions were prepared using demineralized water obtained with a Millipore Milli-Q system (Millipore, Bedford, MA, USA). The pH values were measured using a pH meter (WTW inoLab, Weilheim, Germany) with a WTW SenTix pH electrode.

Synthesis of GO: The synthesis of GO by simplified Hummer's method was previously described in ref. [66]. Briefly, graphite flakes were chemically oxidized with concentrated H_2SO_4 and $KMnO_4$ and stirred vigorously. Oxidation was terminated with the addition of H_2O_2 solution after 10 days. The synthesized GO was then washed three times with 1 M HCl to remove chemical impurities, followed by multiple wash steps with ultrapure water. Finally, the GO solution had a constant pH value of ≈3–4, and the dry weight concentration was measured to be 5.6 g L^{-1}.

Synthesis of rGO-Ag: GO (500 mg) was mixed with silver (I) nitrate solution (10 mM, 500 mL) and stirred for 10 min. Then, sodium borohydride was used as a reducing agent in two different amounts (i.e., 200 and 400 mg) for low (rGO-Ag_L) and high (rGO-Ag_H) reduction levels. The final product was stirred for 24 h and then washed three times with ultrapure water. The final volume was adjusted to 100 mL.

Synthesis of Ag NPs: Ag NPs were synthesized by pouring 0.017% silver nitrate solution into a distilling flask placed on a mineral oil chamber set at 100 °C and stirred at 180 × *g*. An appropriate amount of an aqueous mixture of 4% sodium citrate and 5% tannic acid was added dropwise to the distilling flask and stirred for 15 min, and then the solution was cooled to room temperature. The size of the produced Ag NPs ranged between 5 and 15 nm, as measured by TEM microscopy (Figure S7, Supporting Information).

Characterization of the Synthesized Nanoparticles: The morphology of the synthesized rGO-Ag samples was visualized by using SEM (MAIA 3 SEM (TESCAN Ltd, Brno, Czech Republic)) and TEM (HRTEM FEI Talos F200X). The surface area distribution of rGO-Ag sheets is shown in Figure S6, Supporting Information. The surface charge of the nanoparticles suspended in ultrapure water was determined using a Zetasizer Nano ZS instrument (Malvern Instrument Ltd., Worcestershire, UK). The concentration of Ag present in the rGO-Ag samples was analyzed using a 240 FS AA atomic absorption spectrometer (Agilent

© 2022 The Authors. Advanced Materials Interfaces published by Wiley-VCH GmbH

21967350, 2023, 6, Downloaded from https://onlinelibrary.wiley.com/doi/10.1002/admi.202201996 by Technical University In Brno, Wiley Online Library on [04/08/2023]. See the Terms and Conditions (https://onlinelibrary.wiley.com/terms-and-conditions) on Wiley Online Library for rules of use; OA articles are governed by the applicable Creative Commons License

Technologies, Santa Clara, CA, USA). The nanostructured surface characteristics and the thickness of the synthesized nanomaterials were studied in AFM using Bruker Dimension FastScan microscope (Bruker Nano Surfaces, Santa Barbara, CA, USA). The surface characteristics were also studied using XPS. The oxidation level of GO was determined by studying Raman spectra using a dispersive inVia Reflex Raman microscope (Renishaw, Wotton-under-Edge, UK) with an integrated Leica microscope DM2700 (Leica, Germany). Experimental conditions in detail are described in the Supporting Information.

Cell Culture: HeLa cells (ATCC, CCL-2) and Lenti-X 293T HEK cells (Takara, Japan) were cultured in Dulbecco's Modified Eagle Medium (DMEM) containing 10% fetal bovine serum (FBS) (Invitrogen Corporation, France) and 100 U mL^{-1} penicillin and streptomycin (P/S) antibiotics. THP-1 cells (ATCC, TIB-202) were cultured in RPMI-1640 medium supplemented with 10% FBS and P/S antibiotics. All cell lines were maintained at 37 °C in a humidified atmosphere containing 5% CO_2.

HIV-1 Pseudovirus Production and Infection: For HIV-1 PSV production, 4×10^6 HEK 293T cells were seeded on 100 mm diameter plastic Petri culture dishes in complete DMEM. The next day, the cells were co-transfected with the VSV-G-encoding plasmid pMD2-G (3 µg), packaging plasmid pCMV_dR8.91 (6 µg), and transfer vector pSicoR-luciferase (12 µg) or pSicoR-eGFP using jetPEI (PolyPlus transfection, France) according to the supplier's recommendations. For IN-sfGFP-containing PSV particles, the cells were co-transfected with pMD2-G (2 µg), pCMV-dR8.91 (6 µg), and pSicoR (3 µg), and a plasmid coding for Vpr-IN-sfGFP (4 µg).[42] This construct contained a protease cleavage site inserted between Vpr and Integrase fused to sfGFP (IN-sfGFP). During the maturation of the viral particle, the action of the viral protease led to IN-sfGFP release. The infectivity of these fluorescent PSV particles was comparable to that of non-fluorescent PSV particles.[42] The medium was changed 8 h post-transfection. At 48 h post-transfection, the cell supernatant was collected, filtered through 0.45 µm low binding filters (Millipore, France) to eliminate large cellular debris, and concentrated by centrifugation in Vivaspin collection tubes with a cutoff of 50 kDa (Sartorius, Intec, France). The equivalent p24 concentration was measured by the anti-p24 ELISA test (Takara, Japan).

For the infection, an equivalent of 9 ng of p24 was diluted in 1 mL of complete medium and incubated for 90 min with different amounts of graphene nanocomposites. This concentration was used because it resulted in the infection of ≈70% of HeLa cells and 30% of THP-1 cells. The samples were centrifuged at 1530 × g for 5 min, and the PSV-containing supernatants were deposited on the cells in the presence of polybrene (8 µg mL^{-1}). For luciferase activity measurements, HeLa cells were deposited in 96-well plates at a density of 8000 cells in 100 µL of complete medium. THP-1 cells were seeded in 12-well plates with 2.5×10^4 cells per well. The next day, the rGO-Ag-treated or untreated PSV particles (9 ng mL^{-1} p24 viral antigen) were mixed with polybrene solution (8 µg mL^{-1}) and deposited on the cells. At 24 h post-infection, the cells were lysed using cell culture passive lysis buffer (Promega, France) supplemented with 0.5% Triton X-100 for 20 min at room temperature. The luciferase activity in the cells was measured by a luciferase assay (Promega, France) using a Berthold TriStar luminometer (LB941, Berthold Technologies, Germany). All experiments were performed in triplicate and for at least three independent infections.

MTT Cytotoxicity Assay: To determine the cytotoxicity of the synthesized nanomaterials to mammalian cells, HeLa and THP-1 cells were seeded in 96-well and 12-well plates, respectively. The cells were exposed to varying concentrations of GO, Ag NPs, or rGO-Ag. After 24 h, the cells were thoroughly washed with PBS to remove the nanomaterials and incubated with 3-(4,5-dimethylthiazol-2-yl)-2,5-diphenyl tetrazolium bromide (MTT) (0.5 mg mL^{-1}) (Alpha Aesar, Haverhill, MA, USA) solution in complete media at 37 °C for 3 h. The cells were again thoroughly washed with PBS and DMSO (150 µL) was added to dissolve the formazan crystals. The absorbance at 560 nm was measured using a Xenius plate reader (Safas, Monaco).

Immunoblotting Analysis: Cells were harvested by scraping, and whole-cell lysates were prepared using RIPA buffer (50 mM Tris-HCl, pH 8, 150 mM NaCl, 1% Triton X-100, 1% sodium deoxycholate, 0.1% SDS, and 2 mM $MgCl_2$) supplemented with freshly prepared protease inhibitor cocktail (Roche). The total protein amount in the lysate was quantified using Bradford's reagent, and western blotting was performed using a standard protocol. The results of immunoblotting were visualized on an ImageQuant LAS 4000 (GE Healthcare) using a Bio-Rad HRP Substrate Kit (Cat. #1721064) according to the manufacturer's instructions. The antibodies used were anti-Integrase (Santa Cruz Biotechnology, sc-69721), anti-GFP (Invitrogen, G103362), anti-tubulin (Proteintech, 112224-1-AP), anti-GAPDH (Millipore, MAB374), and secondary HRP conjugated antibody (Promega, W402B, and W401B).

Flow Cytometry Analysis: To quantify the GFP-expressing cell fraction, THP-1 monocytes were seeded in a 12-well plate at 2.5×10^4 cells per well. An equivalent of 9 ng of p24 of PSV/gfp was incubated with rGO-Ag (100 µg mL^{-1}), and the supernatants were prepared as discussed above, followed by cell infection. At 24 h post-infection, the cells were collected, fixed using 4% PFA for 20 min, and washed with cold PBS. Data acquisition was performed using a FACSCanto Flow cytometer (BD Biosciences) and analyzed using FlowJo software (version 10.4). The median fluorescent GFP intensity was used to compare the different conditions in three independent experiments.

SEM Microscopy: For SEM observation, the HIV-1 PSV particles were incubated in the presence of rGO-Ag (200 µg mL^{-1}) for 1.5 h. The larger particles were removed by centrifugation (1530 × *g*, 5 min). Control samples were prepared by the same protocol without rGO-Ag. To image single viral particles, the supernatants were ultracentrifuged at 100 000 × *g* at 4 °C for 30 min, and the PSV-containing pellet was resuspended in PBS (50 µL) and deposited on collagen-treated glass coverslips. After 30 min, the samples were fixed with cacodylate buffer supplemented with 2.5% glutaraldehyde and 2.5% paraformaldehyde for 24 h at 4 °C. For the SEM imaging of the PSV particles attached to the cell surface, the PSV supernatant was deposited on HeLa cells and incubated for 1 h at 4 °C. The cells were then washed and fixed in cacodylate buffer supplemented with 2.5% glutaraldehyde and 2.5% paraformaldehyde for 24 h at 4 °C. Following this fixation, all SEM samples were fixed in 1% osmium tetroxide for 1 h at 4 °C, dehydrated through graded ethanol solutions (50% to 100%), dried (Bal-Tec CPD 030), and finally coated with palladium (Bal-Tec SCD 005). SEM images were acquired using an FEI XL FEG SIRION scanning electron microscope.

Confocal Imaging: A total of 10^5 HeLa cells were seeded in 4-well Ibidi dishes (Ibidi, Germany). The following day, the cells were infected with 300 ng eq. p24 of IN-eGFP-containing PSV particles that were previously incubated with rGO-Ag NCs. 2 h post-infection, the cells were fixed with 4% paraformaldehyde solution. The cell nuclei were stained with Hoechst 33 258 (Sigma–Aldrich, St. Louis, MO, USA). Image acquisition was performed with a Leica TE confocal microscope. Hoechst and eGFP were excited with 405 and 488 nm laser lines, respectively. The emitted fluorescence signals were detected in the spectral ranges of 415–450 nm for Hoechst and 500–550 nm for eGFP. THP-1 cells were imaged with the same microscope settings in channel µ-Slides (Ibidi, Germany), which enabled their immobilization.

For rGO-Ag imaging, HeLa cells were seeded as described above and incubated for 3 or 24 h with the supernatant of samples that initially contained 100 µg mL^{-1} rGO-Ag. The samples were excited with a 561 nm laser line, and the fluorescence signal was detected in the spectral range of 650–750 nm.

Lipid Peroxidation Assay and Time-Lapse Imaging: To study the lipid peroxidation induced by rGO-Ag, 1.5×10^5 293T-HEK cells were seeded in 35 mm Ibidi dishes (Ibidi, Germany). Cells were then treated with the supernatants of samples containing rGO-Ag (50 and 100 µg mL^{-1}) or left untreated. At 24 h post-treatment, the cells were washed and stained with Liperfluo dye (Dojindo) (1 µM) for 30 min at 37 °C, according to the manufacturer's protocol. Fluorescence imaging was performed using a Leica TE confocal microscope. Similarly, PSV particles were treated with rGO-Ag, stained for 30 min with Liperfluo dye (1 µM), ultracentrifuged, and imaged in channel µ-Slides (Ibidi, Germany). The samples were excited with a 488 nm laser line, and the fluorescence signal was detected in the 500–550 nm range. The time-lapse videos of labeled PSVs were acquired by using Leica DMIRE 2 epifluorescence microscope equipped

© 2022 The Authors. Advanced Materials Interfaces published by Wiley-VCH GmbH

21967350, 2023, 6, Downloaded from https://onlinelibrary.wiley.com/doi/10.1002/admi.202201996 by Technical University In Brno, Wiley Online Library on [04/08/2023]. See the Terms and Conditions (https://onlinelibrary.wiley.com/terms-and-conditions) on Wiley Online Library for rules of use; OA articles are governed by the applicable Creative Commons License

with 63× objective (Leica, NA 1.2) and Photometrics prime camera for detection. The image sequences were acquired with an exposure time of 50 ms. The excitation light and detected fluorescence signal was filtered by FITC filtered cube.

Quantitative Reverse Transcription–Polymerase Chain Reaction Assay: Total RNA was extracted from cells using an RNeasy mini kit (Qiagen, France) according to the manufacturer's instructions. The extracted RNA sample concentrations were determined using an ND-1000 NanoDrop spectrophotometer (Labtech, Palaiseau, France). 1 µg of extracted RNA was used for cDNA synthesis using the iScript cDNA synthesis kit (BioRad) according to the manufacturer's instructions. The primers for IL-6, IL-8, TNFα, and IL-1β were obtained from Eurofins Genomics, and the primer for IFN-α was obtained from Qiagen. The sequences are summarized in Table S1, Supporting Information. 50 ng of reverse-transcribed RNA were analyzed with Fast SyberGreen (Applied Biosystems) in triplicate using the StepOne plus 96-well real-time PCR system. qRT–PCR data were analyzed using StepOne Plus software. Target cDNA expression was quantified using the comparative $\Delta\Delta Ct$ (delta–delta CT) method with 18S rRNA as an internal control (housekeeping gene). The obtained data are represented as the mean ± standard error of the mean (S_E).

Statistical Analysis: Statistical analysis of microscopy imaging data was performed by using Origin 2015 software. For Figure 6 j,i, the box plot represents 25–75% of the data, the mean value is highlighted with a bold line, and the whisker represents the standard deviation (SD). The data were tested by a two-sided, Student's *t*-test. The sample size for each experiment is specified in the figure legend. Statistical analysis of RT-qPCR data was carried out using GraphPad software. Two-sided Student's *t*-test was performed on all datasets. In all cases, the difference was considered significant for p values ≤0.05 (*), $p \leq 0.01$(**), and $p \leq 0.001$ (***).

Supporting Information

Supporting Information is available from the Wiley Online Library or from the author.

Acknowledgements

The Vpr-IN-sfGFP plasmid was developed by the group of Prof. A. Cereseto at the Centre for Integrative Biology (CIBIO) at the University of Trento (Trento, Italy) and was generously provided by Dr. A. Francis and Prof. G. Melikyan (Division of Infectious Disease, Department of Pediatrics, Emory University School of Medicine, Children's Healthcare of Atlanta).[42,67] The authors acknowledge Dr. Eleonore Real for optimizing the protocol for HIV-1 pseudovirus production. This work was supported by Fond Régional de Coopération pour la Recherche Région Grand Est (EpiARN Project) and by Institut Universitaire de France (IUF). Y.M. is grateful for their support and provision of additional time to be dedicated to research. CIISB, Instruct-CZ Centre of Instruct-ERIC EU consortium, funded by MEYS CR infrastructure project LM2018127 and European Regional Development Fund-Project "UP CIISB" (No. CZ.02.1.01/0.0/0.0/18_046/0015974), is gratefully acknowledged for the financial support for the measurements performed at the CF Nanobiotechnology. The authors acknowledge the assistance provided by the Research Infrastructure NanoEnviCz, supported by the Ministry of Education, Youth and Sports of the Czech Republic under Project No. LM2018124 and CzechNanoLab Research Infrastructure supported by MEYS CR (LM2018110). This work was supported by ERFD "Multidisciplinary research to increase application potential of nanomaterials in agricultural practice" (No. CZ.02.1.01/0.0/0.0/16_025/0007314). S.M. was supported by Erasmus + Internship.

Conflict of Interest

The authors declare no conflict of interest.

Data Availability Statement

The data that support the findings of this study are available from the corresponding author upon reasonable request.

Keywords

antiviral activity, graphene oxide, human immunodeficiency virus-1, immune response, lipid peroxidation, silver nanoparticles

Received: September 8, 2022
Revised: October 31, 2022
Published online: December 9, 2022

[1] G. Gonçalves, M. Vila, M.-T. Portolés, M. Vallet-Regi, J. Gracio, P. A. A. P. Marques, *Adv. Healthcare Mater.* **2013**, *2*, 1072.
[2] J. M. Yoo, J. H. Kang, B. H. Hong, *Chem. Soc. Rev.* **2015**, *44*, 4835.
[3] S. Mukherjee, Z. Bytesnikova, A. M. Ashrafi, V. Adam, L. Richtera, *Processes* **2020**, *8*, 1636.
[4] C. N. R. Rao, A. K. Sood, R. Voggu, K. S. Subrahmanyam, *J. Phys. Chem. Lett.* **2010**, *1*, 572.
[5] V. Singh, D. Joung, L. Zhai, S. Das, S. I. Khondaker, S. Seal, *Prog. Mater. Sci.* **2011**, *56*, 1178.
[6] H. Y. Mao, S. Laurent, W. Chen, O. Akhavan, M. Imani, A. A. Ashkarran, M. Mahmoudi, *Chem. Rev.* **2013**, *113*, 3407.
[7] K. S. Novoselov, V. I. Fal'ko, L. Colombo, P. R. Gellert, M. G. Schwab, K. Kim, *Nature* **2012**, *490*, 192.
[8] M. Xu, T. Liang, M. Shi, H. Chen, *Chem. Rev.* **2013**, *113*, 3766.
[9] K. S. Novoselov, A. K. Geim, S. V. Morozov, D. Jiang, Y. Zhang, S. V. Dubonos, I. V. Grigorieva, A. A. Firsov, *Science* **2004**, *306*, 666.
[10] L. Feng, Z. Liu, *Nanomedicine* **2011**, *6*, 317.
[11] S. Park, R. S. Ruoff, *Nat. Nanotechnol.* **2009**, *4*, 217.
[12] D. Luo, G. Zhang, J. Liu, X. Sun, *J. Phys. Chem. C* **2011**, *115*, 11327.
[13] J. Yan, L. Chen, C.-C. Huang, S.-C. C. Lung, L. Yang, W.-C. Wang, P.-H. Lin, G. Suo, C.-H. Lin, *Colloids Surf., B* **2017**, *153*, 300.
[14] S. Liu, T. H. Zeng, M. Hofmann, E. Burcombe, J. Wei, R. Jiang, J. Kong, Y. Chen, *ACS Nano* **2011**, *5*, 6971.
[15] V. T. H. Pham, V. K. Truong, M. D. J. Quinn, S. M. Notley, Y. Guo, V. A. Baulin, A.l Kobaisi, C. M. , J. R. , E. P. Ivanova, *ACS Nano* **2015**, *9*, 8458.
[16] S. Ye, K. Shao, Z. Li, N. Guo, Y. Zuo, Q. Li, Z. Lu, L. Chen, Q. He, H. Han, *ACS Appl. Mater. Interfaces* **2015**, *7*, 21571.
[17] T. Du, J. Lu, L. Liu, N. Dong, L. Fang, S. Xiao, H. Han, *ACS Appl. Bio Mater* **2018**, *1*, 1286.
[18] D. Xiang, Q. Chen, L. Pang, C. Zheng, *J. Virol. Methods* **2011**, *178*, 137.
[19] M. Sametband, I. Kalt, A. Gedanken, R. Sarid, *ACS Appl. Mater. Interfaces* **2014**, *6*, 1228.
[20] O. Akhavan, E. Ghaderi, *ACS Nano* **2010**, *4*, 5731.
[21] W. Hu, C. Peng, W. Luo, M. Lv, X. Li, D. Li, Q. Huang, C. Fan, *ACS Nano* **2010**, *4*, 4317.
[22] A. F. de Faria, D. S. T. Martinez, S. M. M. Meira, A. C. M. de Moraes, A. Brandelli, A. G. S. Filho, O. L. Alves, *Colloids Surf., B* **2014**, *113*, 115.
[23] S. Gurunathan, J. W. Han, A. A. Dayem, V. Eppakayala, J.-H. Kim, *Int. J. Nanomed.* **2012**, *7*, 5901.
[24] S. Liu, M. Hu, T. H. Zeng, R. Wu, R. Jiang, J. Wei, L. Wang, J. Kong, Y. Chen, *Langmuir* **2012**, *28*, 12364.
[25] Á. Serrano-Aroca, K. Takayama, A. Tuñón-Molina, M. Seyran, S. S. Hassan, P. P. Choudhury, V. N. Uversky, K. Lundstrom, P. Adadi, G. Palù, A. A. A. Aljabali, G. Chauhan, R. Kandimalla, M. M. Tambuwala, A. Lal, T. M. A. El-Aziz, S. Sherchan, D. Barh,

© 2022 The Authors. Advanced Materials Interfaces published by Wiley-VCH GmbH

21967350, 2023, 6, Downloaded from https://onlinelibrary.wiley.com/doi/10.1002/admi.202201996 by Technical University In Brno, Wiley Online Library on [04/08/2023]. See the Terms and Conditions (https://onlinelibrary.wiley.com/terms-and-conditions) on Wiley Online Library for rules of use; OA articles are governed by the applicable Creative Commons License

E. M. Redwan, N. G. Bazan, Y. K. Mishra, B. D. Uhal, A. Brufsky, *ACS Nano* **2021**, *15*, 8069.
[26] F. Perreault, A. F. de Faria, S. Nejati, M. Elimelech, *ACS Nano* **2015**, *9*, 7226.
[27] K. Krishnamoorthy, M. Veerapandian, L.-H. Zhang, K. Yun, S. J. Kim, *J. Phys. Chem. C* **2012**, *116*, 17280.
[28] Y. Tu, M. Lv, P. Xiu, T. Huynh, M. Zhang, M. Castelli, Z. Liu, Q. Huang, C. Fan, H. Fang, R. Zhou, *Nat. Nanotechnol.* **2013**, *8*, 594.
[29] F. Zou, H. Zhou, D. Y. Jeong, J. Kwon, S. U. Eom, T. J. Park, S. W. Hong, J. Lee, *ACS Appl. Mater. Interfaces* **2017**, *9*, 1343.
[30] J. V. Rogers, C. V. Parkinson, Y. W. Choi, J. L. Speshock, S. M. Hussain, *Nanoscale Res. Lett.* **2008**, *3*, 129.
[31] P. Orłowski, A. Kowalczyk, E. Tomaszewska, K. Ranoszek-Soliwoda, A. Węgrzyn, J. Grzesiak, G. Celichowski, J. Grobelny, K. Eriksson, M. Krzyzowska, *Viruses* **2018**, *10*, 524.
[32] B. Salesa, Á. Serrano-Aroca, *Coatings* **2021**, *11*, 414.
[33] B. Salesa, M. Assis, J. Andrés, *Biomedicines* **2021**, *9*, 1155.
[34] W. J. Stark, *Angew. Chem., Int. Ed.* **2011**, *50*, 1242.
[35] Q. Mu, G. Jiang, L. Chen, H. Zhou, D. Fourches, A. Tropsha, B. Yan, *Chem. Rev.* **2014**, *114*, 7740.
[36] Y.-N. Chen, Y.-H. Hsueh, C.-T. Hsieh, D.-Y. Tzou, P.-L. Chang, *Int. J. Environ. Res. Public Health* **2016**, *13*, 430.
[37] A. C. Ferrari, J. C. Meyer, V. Scardaci, C. Casiraghi, M. Lazzeri, F. Mauri, S. Piscanec, D. Jiang, K. S. Novoselov, S. Roth, A. K. Geim, *Phys. Rev. Lett.* **2006**, *97*, 187401.
[38] J. C. S. Filho, E. C. Venancio, S. C. Silva, H. Takiishi, L. G. Martinez, R. A. Antunes, *SN Appl. Sci.* **2020**, *2*, 1450.
[39] N. Díez, A. Śliwak, S. Gryglewicz, B. Grzyb, G. Gryglewicz, *RSC Adv.* **2015**, *5*, 81831.
[40] A. Shaikh, S. Parida, S. Böhm, *RSC Adv.* **2016**, *6*, 100383.
[41] D. Li, W. Zhang, X. Yu, Z. Wang, Z. Su, G. Wei, *Nanoscale* **2016**, *8*, 19491.
[42] A. C. Francis, C. Di Primio, V. Quercioli, P. Valentini, A. Boll, G. Girelli, F. Demichelis, D. Arosio, A. Cereseto, *AIDS Res. Hum. Retroviruses* **2014**, *30*, 717.
[43] R. Li, L. M. Guiney, C. H. Chang, N. D. Mansukhani, Z. Ji, X. Wang, Y.-P. Liao, W. Jiang, B. Sun, M. C. Hersam, A. E. Nel, T. Xia, *ACS Nano* **2018**, *12*, 1390.
[44] J. Ma, R. Liu, X. Wang, Q. Liu, Y. Chen, R. P. Valle, Y. Y. Zuo, T. Xia, S. Liu, *ACS Nano* **2015**, *9*, 10498.
[45] J. Shang, L. Ma, J. Li, W. Ai, T. Yu, G. G. Gurzadyan, *Sci. Rep.* **2012**, *2*, 792.
[46] H. C. Schniepp, J.-L. Li, M. J. McAllister, H. Sai, M. Herrera-Alonso, D. H. Adamson, R. K. Prud'homme, R. Car, D. A. Saville, I. A. Aksay, *J. Phys. Chem. B* **2006**, *110*, 8535.
[47] Z.-S. Wu, W. Ren, L. Gao, B. Liu, C. Jiang, H.-M. Cheng, *Carbon N Y* **2009**, *47*, 493.
[48] N. M. Dat, D. B. Thinh, L. M. Huong, N. T. Tinh, N. T. T. Linh, N. D. Hai, N. D. Viet, N. T. Dat, M. T. Phong, N. H. Hieu, *Mater Today Chem.* **2022**, *23*, 100738.
[49] N. M. Dat, T. H. Quan, D. M. Nguyet, T. N. M. Anh, D. B. Thinh, T. C. Diep, L. A. Huy, L. T. Tai, N. D. Hai, P. T. Khang, H. M. Nam, M. T. Phong, N. H. Hieu, *Appl. Surf. Sci.* **2021**, *551*, 149434.
[50] J. L. Elechiguerra, J. L. Burt, J. R. Morones, A. Camacho-Bragado, X. Gao, H. H. Lara, M. J. Yacaman, *J. Nanobiotechnol.* **2005**, *3*, 6.
[51] C. Carlson, S. M. Hussain, A. M. Schrand, L. K. Braydich-Stolle, K. L. Hess, R. L. Jones, J. J. Schlager, *J. Phys. Chem. B* **2008**, *112*, 13608.
[52] A. R. Gliga, S. Skoglund, I. O. Wallinder, B. Fadeel, H. L. Karlsson, *Part. Fibre Toxicol.* **2014**, *11*, 11.
[53] M. I. Sriram, K. Kalishwaralal, S. Barathmanikanth, S. Gurunathani, *Nanosci. Methods* **2012**, *1*, 56.
[54] T. Kathiraven, A. Sundaramanickam, N. Shanmugam, T. Balasubramanian, *Appl. Nanosci.* **2015**, *5*, 499.
[55] G. Bagherzade, M. M. Tavakoli, M. H. G. Namaei, *Asian Pac. J. Trop. Biomed.* **2017**, *7*, 227.
[56] J. Zhang, H.-Y. Cao, J.-Q. Wang, G.-D. Wu, L. Wang, *Front. Cell Dev. Biol.* **2021**, *9*, 616888.
[57] C. Richter, *Chem. Phys. Lipids* **1987**, *44*, 175.
[58] C. de la Haba, J. R. Palacio, P. Martínez, A. Morros, *Biochim. Biophys. Acta, Biomembr.* **2013**, *1828*, 357.
[59] R. Schlegel, T. S. Tralka, M. C. Willingham, I. Pastan, *Cell* **1983**, *32*, 639.
[60] J. L. Anderson, T. J. Hope, *Gene Ther.* **2005**, *12*, 1667.
[61] A. Piperno, A. Scala, A. Mazzaglia, G. Neri, R. Pennisi, M. T. Sciortino, G. Grassi, *Int. J. Mol. Sci.* **2018**, *19*, 3365.
[62] S. P. Mukherjee, M. Bottini, B. Fadeel, *Front Immunol.* **2017**, *8*, 673.
[63] G. Qu, S. Liu, S. Zhang, L. Wang, X. Wang, B. Sun, N. Yin, X. Gao, T. Xia, J.-J. Chen, G.-B. Jiang, *ACS Nano* **2013**, *7*, 5732.
[64] C. Hoyle, J. Rivers-Auty, E. Lemarchand, S. Vranic, E. Wang, M. Buggio, N. J. Rothwell, S. M. Allan, K. Kostarelos, D. S. Brough, *ACS Nano* **2018**, *12*, 11949.
[65] S. P. Mukherjee, K. Kostarelos, B. Fadeel, *Adv. Healthcare Mater.* **2018**, *7*, 1700815.
[66] A. Đurović, Z. Stojanović, Z. Bytešníková, S. Kravić, P. Švec, J. Přibyl, L. Richtera, *J. Mater. Sci.* **2022**, *57*, 5533.
[67] A. Albanese, D. Arosio, M. Terreni, A. Cereseto, *PLoS One* **2008**, *3*, e2413.

© 2022 The Authors. Advanced Materials Interfaces published by Wiley-VCH GmbH

21967350, 2023, 6, Downloaded from https://onlinelibrary.wiley.com/doi/10.1002/admi.202201996 by Technical University In Brno, Wiley Online Library on [04/08/2023]. See the Terms and Conditions (https://onlinelibrary.wiley.com/terms-and-conditions) on Wiley Online Library for rules of use; OA articles are governed by the applicable Creative Commons License